ISSN 0021-3640, JETP Letters, 2017, Vol. 105, No. 12, pp. 806–817. © Pleiades Publishing, Inc., 2017.
Original Russian Text © A.L. Rakhmanov, K.I. Kugel, M.Yu. Kagan, A.V. Rozhkov, A.O. Sboychakov, 2017, published in Pis'ma v Zhurnal Eksperimental'noi i Teoreticheskoi Fiziki, 2017, Vol. 105, No. 12, pp. 768–779.

SCIENTIFIC SUMMARIES

Inhomogeneous Electron States in the Systems with Imperfect Nesting

A. L. Rakhmanov[a, b, c], K. I. Kugel[a, e, *], M. Yu. Kagan[d, e], A. V. Rozhkov[a, b], and A. O. Sboychakov[a]

[a] *Institute for Theoretical and Applied Electrodynamics, Russian Academy of Sciences, Moscow, 125412 Russia*
[b] *Moscow Institute for Physics and Technology (State University), Dolgoprudnyi, Moscow region, 141700 Russia*
[c] *All-Russia Research Institute of Automatics, Moscow, 127055 Russia*
[d] *Kapitza Institute for Physical Problems, Russian Academy of Sciences, Moscow, 119334 Russia*
[e] *National Research University Higher School of Economics, Moscow, 101000 Russia*
**e-mail: kugel@orc.ru*

Received May 11, 2017

A brief overview of the theoretical studies on the electronic phase separation in the systems with the imperfect nesting of Fermi surface sheets is presented. Among these systems, there are chromium and its alloys, superconducting iron-based pnictides, bilayer graphene, and some other materials.

DOI: 10.1134/S0021364017120116

1. INTRODUCTION

Among the multiband materials with a tendency to electronic phase separation, there exists an important family of systems with the nesting of the Fermi surface. The Fermi surface nesting is a very popular and important concept in condensed matter physics [1]. The existence of two fragments of the Fermi surface, which can be matched upon translation by a certain reciprocal lattice vector ($\mathbf{Q}_0$), entails an instability of a Fermi liquid state giving rise to an additional order parameter. The nesting is widely invoked for the analysis of charge density wave (CDW) states [2, 3], spin density wave (SDW) states [4, 5], mechanisms of high-T_c superconductivity (HTSC) [6–8], antiferromagnetism of chromium and its alloys [9–12], etc. It is important to emphasize that the nesting in a real material may be imperfect; i.e., the Fermi surface fragments can match only approximately via the translation by the $\mathbf{Q}_0$ vector. Quite recently, it was demonstrated that the imperfect-nesting mechanism can be responsible for the nanoscale phase separation in chromium alloys [13], in iron-based superconductors [14], and in doped bilayer graphene [15, 16]. In this context, the studies of spin and charge inhomogeneities related to the imperfect nesting are currently especially active in the physics of low-dimensional compounds [17–19].

Physical mechanisms underlying the nucleation of the inhomogeneous state in the systems with nesting are the following. The electronic spectrum instability related to the nesting gives rise to a new order parameter. Hence, the free energy of the system becomes lower. The better the nesting, the larger is this energy gain. Thus, it may be favorable for the system to break up into two phases with the better and worse (or even absent) nesting and having different densities of itinerant electrons.

2. RICE MODEL. PHASE SEPARATION IN CHROMIUM AND ITS ALLOYS

We start with the model proposed by Rice [12] to describe the incommensurate antiferromagnetism in chromium and its alloys (see also review [20]). On one hand, this model is rather simple and allows for a detailed examination of its phase diagram. On the other hand, it can be applied to describe important real systems.

The model band structure corresponds to two spherical pockets of the Fermi surface, electron and hole ones. The radii of these pockets may be different. It includes as well another band or bands, which do not participate in the magnetic ordering (nonmagnetic bands). All interactions are ignored except the repulsion between electrons and holes in the pockets giving rise to the ordering since even a small coupling in this channel generates a band instability and opens a gap in the electron spectrum. The system we study is a three-dimensional one. Its Hamiltonian has the form

$$\hat{H} = \sum_{\mathbf{k},\sigma,\alpha} \epsilon^{\alpha}(\mathbf{k}) n^{\alpha}_{\mathbf{k}\sigma} + V \sum_{\mathbf{k},\mathbf{k}',\mathbf{q},\sigma,\sigma'} a^{\dagger}_{\mathbf{k}+\mathbf{q}\sigma} a_{\mathbf{k}\sigma} b^{\dagger}_{\mathbf{k}'-\mathbf{q}\sigma'} b_{\mathbf{k}'\sigma'}, \quad (1)$$

where α is equal to a (electrons), b (holes), and c ("nonmagnetic" charge carriers); $a^{\dagger}$ and $b^{\dagger}$ are the

creation operators for electrons and holes, respectively; n is the number operator; and V is the Coulomb repulsion, and σ is the spin projection. The "nonmagnetic" charge carriers have the density of states N_r at the Fermi energy. The energy spectra for electrons and holes near the Fermi energy can be written in the form

$$\begin{aligned}\epsilon^a_{\mathbf{k}} &= \hbar v_F(k - k_{Fa}) = \hbar v_F(k - k_F) - \mu,\\ \epsilon^b_{\mathbf{k}+\mathbf{Q}_0} &= -\hbar v_F(k - k_{Fb}) = -\hbar v_F(k - k_F) - \mu,\end{aligned} \tag{2}$$

where $k_F = (k_{Fa} + k_{Fb})/2$, $\mu = \hbar v_F(k_{Fa} - k_{Fb})/2$ is the chemical potential, and vector $\mathbf{Q}_0$ connects the centers of electron and hole pockets in the momentum space.

We consider the weak-coupling regime: $VN_m \ll 1$, where $N_m = k_F^2/2\pi^2\hbar v_F$. If the radii of electron and hole pockets are identical (perfect nesting), we have $\mu = 0$. Performing the standard BCS-like calculations, we find that the ground state at $\mu = 0$ corresponds to the antiferromagnetic (AFM) order parameter $\Delta_0 = \epsilon_F \exp(-1/N_m|V|) \ll \epsilon_F = \hbar v_F k_F$. The order parameter Δ_0 couples charge carriers with unequal momenta. Consequently, in the real space, the order parameter Δ_0 corresponds to the rotation of the magnetization axis related to the wave vector $\mathbf{Q}_0$. Usually, the electron and hole pockets are located at the high-symmetry points of the Brillouin zone and the vector $\mathbf{Q}_0$ is the reciprocal lattice vector. This AFM ordering is usually referred to as the commensurate one.

If $\mu \neq 0$, the electron and hole Fermi spheres have different radii and do not coincide upon a translation. However, if μ is small, the difference between the spheres remains small, and we can define a new nesting vector $\mathbf{Q}_1 = \mathbf{Q}_0 + \mathbf{Q}$, which corresponds to the minimum energy of the spin density wave. Hence, $\mathbf{Q}$ becomes an additional optimization parameter. The SDW order parameter can be written as

$$\Delta = V\sum_{\mathbf{k}}\langle a^\dagger_{\mathbf{k}\sigma} b_{\mathbf{k}+\mathbf{Q}_1-\sigma}\rangle. \tag{3}$$

Vector $\mathbf{Q}$ is small: $|\mathbf{Q}| \sim |\Delta|/\hbar v_F \ll |\mathbf{Q}_0|$. Thus, the order parameter Δ describes an AFM ordering with a slowly rotating magnetization axis. This rotation is unrelated to the lattice symmetry. Such ordering is referred to as the incommensurate one. Note that the state under study is similar to the Fulde–Ferrell–Larkin–Ovchinnikov (FFLO) state in superconductors [21, 22]. Note also that we can introduce the order parameters of a slightly different structure than that in (3). However, the general results do not change significantly [13, 22, 23]. The difference in the free energy and the chemical potential calculated for different forms of the order parameter is small, and the balance in real systems may be shifted by factors disregarded in the present model (e.g., the anisotropy and disorder) [13].

It is convenient to calculate the equilibrium parameters of the system by the minimization of the thermodynamic potential $\Omega = -T\ln\left[\mathrm{Tr}\exp\left(-\frac{\hat{H} - \mu\hat{N}}{T}\right)\right]$, where $\hat{N}$ is the operator of the total number of particles. In the mean-field approximation, the eigenenergies of Hamiltonian (1) are

$$E_{1,2} = \frac{\epsilon^a_{\mathbf{k}} + \epsilon^b_{\mathbf{k}+\mathbf{Q}_1}}{2} \pm \sqrt{\Delta^2 + \left[\frac{\epsilon^a_{\mathbf{k}} - \epsilon^b_{\mathbf{k}+\mathbf{Q}_1}}{2}\right]^2}. \tag{4}$$

Within the same approximation, the grand potential per unit volume can be written as

$$\begin{aligned}\Omega = \frac{2\Delta^2}{V} - 2T\sum_s\int\frac{d^3\mathbf{k}}{(2\pi)^3}\ln\left(1 + e^{-E_s/T}\right)\\ - 2TN_r\int\ln\left(1 + e^{-(\epsilon-\mu)/T}\right)d\epsilon,\end{aligned} \tag{5}$$

where the first and second terms are the contributions of the "magnetic" electrons, whereas the third term corresponds to "nonmagnetic" charge carriers. To carry out the integration over $\mathbf{k}$, we expand the band energies in powers of $|\mathbf{Q}|$ and $\delta k = |\mathbf{k}| - k_F$:

$$\begin{aligned}\epsilon^b_{\mathbf{k}+\mathbf{Q}_1} + \epsilon^a_{\mathbf{k}} &\approx 2\mu + 2Q\eta,\\ \epsilon^b_{\mathbf{k}+\mathbf{Q}_1} - \epsilon^a_{\mathbf{k}} &\approx 2v_F\delta k + 2Q\eta,\end{aligned} \tag{6}$$

where $Q = v_F|\mathbf{Q}|$ and η is the cosine of the angle between $\mathbf{k}$ and $\mathbf{Q}$. After the integration, we find [13]

$$\begin{aligned}\delta\Omega = \Omega(\Delta, Q, \mu) - \Omega(0, Q, \mu)\\ = \frac{k_F^3}{\pi^2\epsilon_F}\left\{\Delta^2\left(\ln\frac{\Delta}{\Delta_0} - \frac{1}{2}\right) + \frac{Q^2}{3} + \mu^2 + \frac{\pi^2T^2}{3}\right.\\ \left. + T\int_0^\infty d\xi\int_{-1}^1 d\eta\ln\left[f(Q\eta - \mu - \varepsilon)f(\mu - Q\eta - \epsilon)\right]\right\},\end{aligned}$$

where $f(\epsilon) = 1/[1 + \exp(\epsilon/T)]$ is the Fermi distribution function and $\epsilon = \sqrt{\Delta^2 + \xi^2}$. The equations for the equilibrium values of Δ and Q are determined by minimizing $\delta\Omega$ [13]:

$$\begin{aligned}\ln\frac{\Delta_0}{\Delta} &= \int_0^\infty\frac{d\xi}{2\epsilon}\int_{-1}^1 d\eta\left[f(\epsilon + \mu - Q\eta) + f(\epsilon - \mu + Q\eta)\right],\\ \frac{-2Q}{3} &= \int_0^\infty d\xi\int_{-1}^1\eta\, d\eta\left[f(\epsilon + \mu - Q\eta) + f(\epsilon - \mu + Q\eta)\right].\end{aligned} \tag{7}$$

The total number of electrons per unit volume $n(\mu)$ is the sum of magnetic and nonmagnetic contributions $n_m(\mu)$ and $n_r(\mu)$, respectively. The doping level x is $x = n(\mu) - n(0)$. Since T, $\mu \ll \epsilon_F$, we can write $n_r(\mu) - n_r(0) = N_r\mu$. For the magnetic charge carriers,

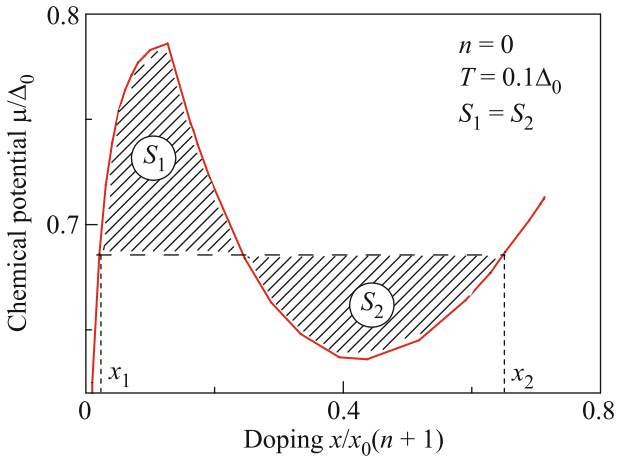

Fig. 1. (Color online) Chemical potential μ versus doping x for the homogeneous SDW phase at $T/\Delta_0 = 0.1$ and $n = 0$ [solid (red) line]. The horizontal dashed line shows the Maxwell construction, with the shaded areas $S_1 = S_2$ (Fig. 3 from [13]).

we have $n_m(\mu) = 2\sum_{\mathbf{k},s} f(E_s(\mathbf{k}))$. After straightforward calculations, we derive

$$\frac{x}{x_0} = \frac{n\mu}{\Delta_0} + \int_0^\infty \frac{d\xi}{\Delta_0}\int_{-1}^{1} d\eta\,[f(\epsilon - \mu + Q\eta) - f(\epsilon + \mu - Q\eta)], \quad (8)$$

where $x_0 = 4\Delta_0 N_m$ and $n = N_r/2N_m$.

The phase diagram of the model can be constructed by the numerical solution of Eqs. (7) and (8).

First, one can calculate the Néel temperature $T_N(x)$ for the homogeneous AFM state of the system and the transition temperature T_Q between the commensurate and incommensurate AFM states. Then, we can determine the region of the inhomogeneous state analyzing the dependence of the grand potential Ω or chemical potential μ versus the doping level x [13].

As an illustration, a typical dependence of the chemical potential on doping for the model under study is shown in Fig. 1. It is seen in this figure that the function $\mu(x)$ has a descending part, which means a negative compressibility and, hence, instability of the homogeneous AFM phase. In the inhomogeneous state, the system is segregated into two phases with different doping levels x_1 and x_2. The values x_1 and x_2 can be found using the Maxwell construction: the horizontal dashed line in Fig. 1 is drawn in such a manner that the areas of the shaded regions S_1 and S_2 are equal.

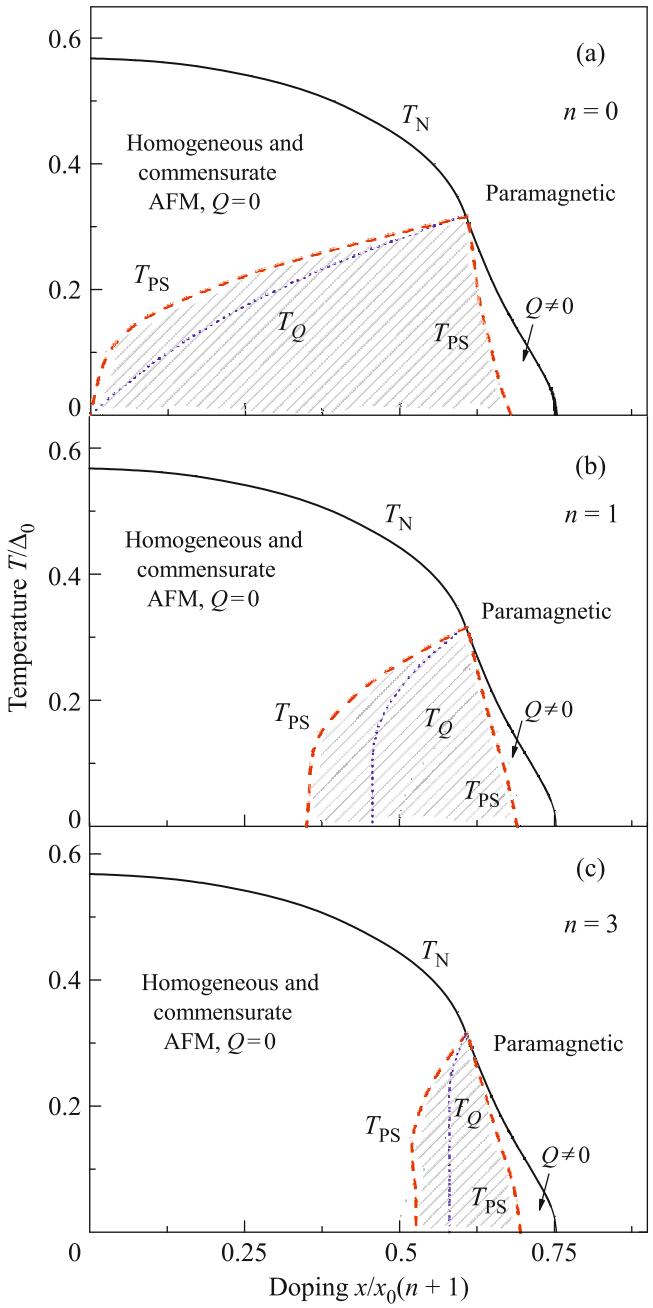

Fig. 2. (Color online) Phase diagram of the model in the (x, T) plane (Fig. 4 from [13]) for $n =$ (a) 0 (no electrons in nonmagnetic pockets), (b) 1, and (c) 3. The solid (black) curves represent the Néel temperature $T_N(x)$, which separates the paramagnetic and AFM phases. The dotted (blue) curves correspond to the boundary between the commensurate and incommensurate homogeneous AFM phases, $T_Q(x)$. The dashed (red) curve, $T_{PS}(x)$, is the boundary between the uniform and phase-separated (shaded areas) states.

In Fig. 2, $T_{PS}(x)$ is a boundary between the homogeneous and phase-separated states in the (x, T) plane shown by the dashed (red) curve. The phase with lower

doping x_1 is the commensurate AFM phase ($Q = 0$), whereas the phase with higher doping x_2 is the incommensurate AFM one ($Q \neq 0$). Thus, the phase separation occurs owing to the competition between two AFM states with different structures.

Above, we have mentioned the mapping between the Rice model and the FFLO superconductor. Indeed, the Zeeman field in the FFLO superconductor corresponds to doping in the Rice model. However, the magnetic field, being an intense thermodynamic quantity, does not allow for phase separation. However, for cold atoms in an optical trap (where an analog of the FFLO is predicted), it may be possible to control not the field, but the polarization, which is an extensive quantity. In this case, phase separation is possible [24]. Note that the FFLO phase is quite sensitive to the disorder [25]. It is natural to expect that the incommensurate AFM order should also be susceptible to the existence of defects.

3. MAGNETIC FIELD EFFECT ON THE PHASE SEPARATION

Naturally, the magnetically ordered system under discussion is especially sensitive to the applied magnetic field. To take into account the magnetic field $\mathbf{B}$, we should first replace the momentum operator $\hat{\mathbf{p}}$ by the gauge invariant combination $\hat{\mathbf{p}} + (e/c)\mathbf{A}$, where $\mathbf{A}$ is the vector potential of the magnetic field. Second, it is necessary to add the Zeeman term $g_\alpha \sigma \hbar \omega_\alpha$ to the one-electron Hamiltonian, where g_α is the Landé g-factor and $\omega_\alpha = eB/cm_\alpha$ is the cyclotron frequency of a charge carrier with the mass m_α. The energy spectrum of the model is now characterized by two single-particle energy scales: the Fermi energy ϵ_F and the distance $\hbar\omega_\alpha$ between the Landau levels. The energy scale related to the electron–hole interaction is characterized by the AFM band gap Δ_0. The Landau quantization is of importance in the high-field range $\hbar\omega_\alpha > \Delta_0$, whereas at low fields, $\hbar\omega_\alpha < \Delta_0$, it can be neglected. Here, we limit ourselves to the regime of low magnetic fields, neglecting any corrections of the order of $\hbar\omega_\alpha/\epsilon_F \ll 1$.

Adding Zeeman terms, we obtain instead of Eqs. (2)

$$\begin{aligned} \epsilon^a_\sigma(\mathbf{k}) &= \hbar v_F(k - k_F) - \mu + g_a \sigma \hbar \omega_a, \\ \epsilon^b_\sigma(\mathbf{k} + \mathbf{Q}_0) &= -\hbar v_F(k - k_F) - \mu + g_b \sigma \hbar \omega_b. \end{aligned} \tag{9}$$

The magnetic field lifts the degeneracy with respect to spin (Fig. 3). Therefore, we have to introduce a two-component order parameter corresponding to the nesting vectors shown by the arrows in Fig. 3. For simplicity, we do not consider the incommensurate SDW ordering. Then, the components of the order parameter can be represented in the form [26]

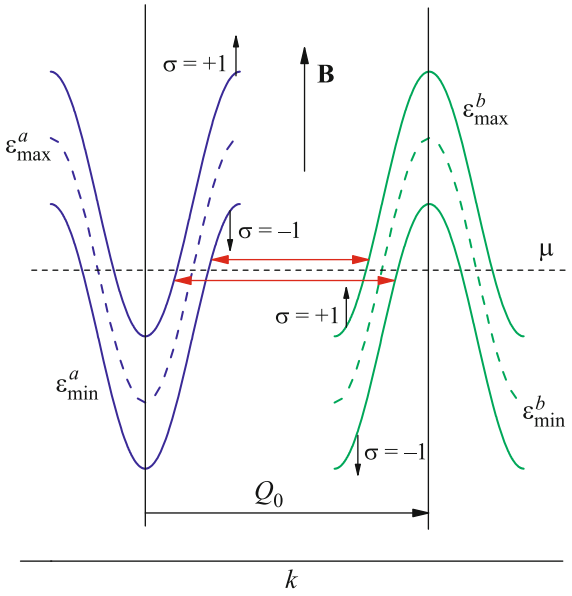

Fig. 3. (Color online) Band structure of the system in an applied magnetic field. The magnetic field lifts the degeneracy of the energy bands with respect to spin. The red arrows indicate the interband coupling giving rise to the order parameters (Fig. 1 from [26]).

$$\Delta_\uparrow = V\sum_{\mathbf{k}} \langle a^\dagger_{\mathbf{k},\uparrow} b_{\mathbf{k},\downarrow} \rangle, \quad \Delta_\downarrow = V\sum_{\mathbf{k}} \langle a^\dagger_{\mathbf{k},\downarrow} b_{\mathbf{k},\uparrow} \rangle. \tag{10}$$

The case where the electron and hole bands are perfectly symmetric is the simplest one. In such a situation, however, the applied magnetic field produces no effect on the electron spectrum. Thus, some electron–hole asymmetry is necessary to obtain a nontrivial result.

Let the effective masses of electrons and holes be equal, $m_a = m_b = m$, and hence $\omega_a = \omega_b = \omega_H$, whereas $g_a \neq g_b$. Following the procedure described in the previous section, now we can find the eigenenergies of the Hamiltonian and calculate the grand potential Ω. Minimization of Ω yields the following equation for the gap Δ [26]:

$$\ln\frac{\Delta_0}{\Delta_\sigma} = \int_0^\infty d\xi \frac{f(\sqrt{\Delta_\sigma^2 + \xi^2} + \mu_\sigma) + f(\sqrt{\Delta_\sigma^2 + \xi^2} - \mu_\sigma)}{\sqrt{\Delta_\sigma^2 + \xi^2}}, \tag{11}$$

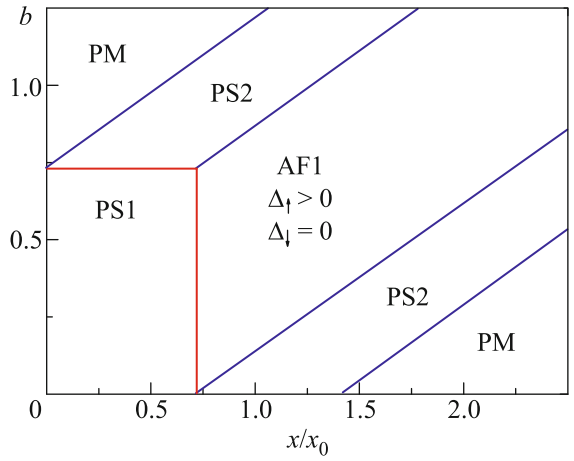

Fig. 4. (Color online) Phase diagram of the system at $T = 0$. In this diagram, we see the homogeneous SDW phase AF1 (definition is given in the main text), two regions with uniform paramagnetic (PM) phase, and phase separated states PS1 (mixture of two SDW phases, see the text) and PS2 (mixture of AF1 and PM phases) (Fig. 3b from [26]).

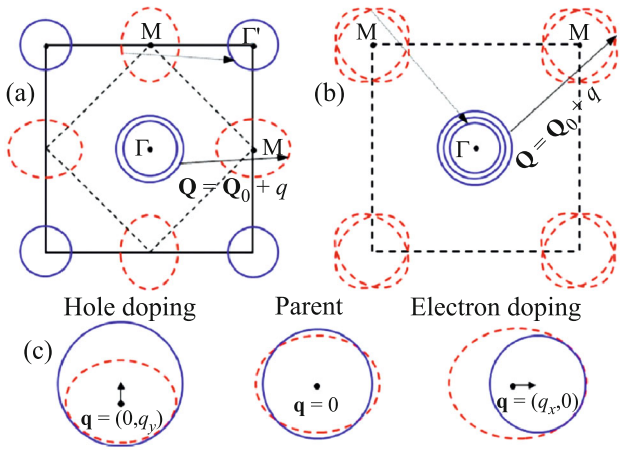

Fig. 5. (Color online) Schematic illustration of the Fermi surface of iron pnictides in the (a) unfolded and (b) folded Brillouin zone. We have three hole pockets located near the center of the folded Brillouin zone [shown by (blue) solid curves]. In the unfolded Brillouin zone, one of the hole pockets moves to the corner of the Brillouin zone. For the unfolded Brillouin zone (a), the electron pockets are elliptic [(red) dashed curves] and located near the $(0, \pi/a)$ and $(\pi/a, 0)$ points, while in the folded Brillouin zone, they are represented by overlapping ellipses located at the corners. Arrows show the possible nesting vectors between hole and electron pockets, which give rise to the SDW order. (c) Schematic illustration of the possible nesting at different doping levels (Fig. 1 from [14]).

where $\mu_\sigma = \mu - \sigma(g_a - g_b)\hbar\omega_H/2$. Neglecting the existence of the nonmagnetic parts of the Fermi surface, we obtain similar to Eq. (8)

$$\frac{x}{x_0} = \sum_\sigma \int_0^\infty \frac{d\xi}{\Delta_0}\left[f(\sqrt{\Delta_\sigma^2 + \xi^2} - \mu_\sigma) - f(\sqrt{\Delta_\sigma^2 + \xi^2} + \mu_\sigma)\right]. \quad (12)$$

The phase diagram of the model on the (B, x) plane at $T = 0$ is shown in Fig. 4 [26], where $b = |g_a - g_b|\hbar\omega_H/2\Delta_0 \propto B$. The homogeneous paramagnetic state exists in the system at a high doping level $(x > 2b - \sqrt{2})$ or at a high applied magnetic field $(b > 1/\sqrt{2} + x/2x_0)$. In the low doping range and at a low magnetic field, the ground state of the system corresponds to the phase separation. The inhomogeneous phase PS1 (see Fig. 4) is a mixture of the two AFM phases. The first phase corresponds to SDW with zero doping and $\Delta_\uparrow = \Delta_\downarrow = \Delta_0$. In the second phase with nonzero doping, we have $\Delta_\uparrow = \Delta_0$ and $\Delta_\downarrow = 0$. This phase is referred to as AF1. The PS1 phase is the ground state of the model if $|b| < 1/\sqrt{2}$ and $|x/x_0| < 1/\sqrt{2}$. The homogeneous AF1 phase is stable within the range of intermediate magnetic fields $x/2x_0 - 2\sqrt{2} < b < x/2x_0 + 2\sqrt{2}$. The inhomogeneous state is stable in the regions between the homogeneous paramagnetic (PM) and AF1 phases. The phase-separated PS2 state consists of the mixture of the SDW AF1 phase and the PM phase. Thus, we see that the magnetic field lifts the spin-projection degeneracy of the SDW order parameter. As a result, the number of possible homogeneous states increases, which, in turn, drastically affects the picture of the electronic phase separation.

4. PHASE SEPARATION IN SUPERCONDUCTING PNICTIDES

Superconducting iron-based pnictides form another system with imperfect nesting. The phase diagram in iron pnictides is very rich and contains the regions corresponding to spin and charge inhomogeneities [27–32]. Note that the electron–electron interaction in pnictides is usually considered to be weak (see, e.g., Section III A in review [33]). The phase separation is also observed in superconducting iron chalcogenides [34, 35]. In these compounds, however, it seems to be related to another mechanism since it is usually assumed that the Fermi surface nesting is absent in chalcogenides.

The Fermi surface of iron pnictides is typically described using two related representations. In Fig. 5a, we plot the Fermi surface within the so-called unfolded Brillouin zone, which corresponds to the square lattice of iron atoms, with one Fe atom per unit cell and having the lattice constant a. In this representation, two quasi-two-dimensional nearly circular hole pockets are centered at the $\Gamma(0, 0)$ point and one

even more circular hole pocket is located near the $\Gamma'(\pi,\pi)$ point. Two elliptical electron pockets are centered at the points $M(0,\pi/a)$ and $M(\pi/a,0)$. The actual unit cell in pnictides contains two Fe atoms located at nonequivalent positions.

The folded Brillouin zone corresponding to this unit cell is obtained by folding the Brillouin zone shown in Fig. 5a by dashed lines and consequent rotation by an angle of $\pi/4$. The Fermi surface in the folded Brillouin zone is shown in Fig. 5b. In this figure, all three hole pockets are located near the point $\Gamma(0,0)$, while electron pockets represented by overlapping ellipses are located near the points $M(\pm\pi/\bar{a},\pi/\bar{a})$ with $\bar{a} = a/\sqrt{2}$. Here, we make several simplifications. First, we neglect the effects associated with nonequivalent positions of the Fe atoms. Consequently, the use of the unfolded Brillouin zone is sufficient. Second, we will neglect the three-dimensional structure of the material and study only the two-dimensional model.

Following [14], the Hamiltonian of the model can be written as $\hat{H} = \hat{H}_0 + \hat{H}_{\rm int}$, where

$$\hat{H}_0 = \sum_{\mathbf{k}\lambda\sigma}\epsilon^h_{\lambda\mathbf{k}}a^\dagger_{\mathbf{k}\lambda\sigma}a_{\mathbf{k}\lambda\sigma} + \sum_{\mathbf{k}s\sigma}\epsilon^e_{s\mathbf{k}}b^\dagger_{\mathbf{k}s\sigma}b_{\mathbf{k}s\sigma}. \quad (13)$$

Here, $a^\dagger_{\mathbf{k}\lambda\sigma}, a_{\mathbf{k}\lambda\sigma}$ ($b^\dagger_{\mathbf{k}s\sigma}, b_{\mathbf{k}s\sigma}$) are the creation and annihilation operators for charge carriers in the holelike (electronlike) bands, $\lambda = 1,2,3$ ($s = 1,2$), with the energies $\epsilon^h_{\lambda\mathbf{k}}$ ($\epsilon^e_{s\mathbf{k}}$). Assuming that the bands have quadratic dispersion laws near the Fermi level, for the holelike bands with the cylindrical Fermi surface, we have

$$\begin{aligned}\epsilon^h_{1\mathbf{k}} &= -\frac{\hbar v^h_{\rm F}(k^2-k_{\rm F}^2)}{2k_{\rm F}} - \mu,\\ \epsilon^h_{2\mathbf{k}} &= -\frac{\hbar v^h_{2\rm F}(k^2-k_{\rm F}^2)}{2k_{\rm F}} - \Delta_2 - \mu,\\ \epsilon^h_{3\mathbf{k}+\bar{\mathbf{Q}}} &= -\frac{\hbar v^h_{3\rm F}(k^2-k_{\rm F}^2)}{2k_{\rm F}} - \Delta_3 - \mu,\end{aligned} \quad (14)$$

where $\hbar v_{\rm F}$ and $\hbar v_{2,3\rm F}$ are the Fermi velocities, $\bar{\mathbf{Q}} = (\pi/a,\pi/a)$, and $\Delta_{2,3}$ determine the difference in the radii of pockets.

The electronlike components of the Fermi surface are elliptic and can be represented as follows [14]:

$$\begin{aligned}\epsilon^e_{1\mathbf{k}+\mathbf{Q}_0} &= \epsilon^e_{1\mathbf{k}+\mathbf{Q}'_0}\\ &= \frac{\hbar v^e_{\rm F}(k^2-k_{\rm F}^2)}{2k_{\rm F}} + \frac{\alpha\hbar v^e_{\rm F}}{k_{\rm F}}(k_x^2-k_y^2) - \mu,\end{aligned} \quad (15)$$

where $\mathbf{Q}_0 = (\pi/a,0)$ and $\mathbf{Q}'_0 = (0,\pi/a)$, and $v^e_{\rm F}$ is the Fermi velocity in electron bands. The parameter α defines the ellipticity of the electron pockets. The major axes of the ellipses are directed toward the point Γ at $\alpha > 0$ and perpendicular to this direction when $\alpha < 0$.

The interaction Hamiltonian $\hat{H}_{\rm int}$ includes a number of contributions. However, since we are interested in the SDW order and the phase separation, the electron–electron and hole–hole interactions can be ignored. It is well known [27] that the local magnetic moment in pnictides oscillates along one of the crystal axes. To reproduce this stripy magnetic structure, it is sufficient to consider the coupling of one electron band and one hole band. For the sake of definiteness, we assume that these are ϵ^h_1 and ϵ^e_1. Then, we have

$$\hat{H}_{\rm int} = V\sum_{\mathbf{k},\mathbf{k}',\mathbf{K},\sigma,\sigma'} a^\dagger_{\mathbf{k}+\mathbf{K}1\sigma}a_{\mathbf{k}1\sigma}b^\dagger_{\mathbf{k}'-\mathbf{K}1\sigma'}b_{\mathbf{k}'1\sigma'}. \quad (16)$$

The described model for pnictides is a generalization of the Rice model. As in the latter case, two bands participate in the magnetic transition, and there is a "reservoir" (nonmagnetic bands). However, the perfect nesting is impossible for pnictides since the form of the hole and electron pockets is different for any doping level.

Since the Coulomb interaction in iron pnictides is weak, $V/\epsilon_{\rm F} \ll 1$, where $\epsilon_{\rm F} = (v^e_{\rm F} + v^h_{\rm F})k_{\rm F}/2$ is the Fermi energy, the problem can be solved in the mean-field approximation [14]. We will search for the order parameter in form (3). The magnetization corresponding to the chosen AFM order lies in the xy plane. For the commensurate SDW case, the magnetization direction remains unchanged when one moves along the direction normal to $\mathbf{Q}_0$. When one moves parallel to $\mathbf{Q}_0$, the magnetization reverses its direction from one iron atom to the next iron atom. For incommensurate SDW, this "stripy" pattern slowly rotates in the xy plane [14].

In the approximation under study, the energy spectrum of Hamiltonian (16) is similar to that given by (4) and the grand potential has form (5), where energies $\epsilon^{a,b}$ involved in expression (4) for E_s should be replaced by $\epsilon^{e,h}$. The minimization of the grand potential Ω gives the equations for Δ and $\mathbf{Q}$ similar to Eqs. (7) [14]. Within the weak coupling scheme, the SDW order arises only if the deviation from the perfect nesting is small, i.e., $\alpha \ll 1$. We also assume that $\Delta/\epsilon_{\rm F}$, $|\mathbf{q}|/k_{\rm F} \ll 1$. Then, the equation for the order parameter at $T = 0$ can be written as [14]

$$\ln\frac{1}{\delta} = \int_0^{2\pi}\frac{d\varphi}{2\pi}\,{\rm Re}\left\{\cosh^{-1}\left[\frac{\nu_0(\mathbf{p},\varphi)-\nu}{\delta}\right]\right\}, \quad (17)$$

where

$$\nu_0(\mathbf{p},\varphi) = p_x\cos\varphi + p_y\sin\varphi - \frac{\bar{\alpha}}{2}\cos 2\varphi,$$
$$\bar{\alpha} = \frac{\alpha\kappa\varepsilon_F}{\Delta_0}, \quad \kappa = \frac{2\sqrt{v_F^e v_F^h}}{v_F^e + v_F^h}, \quad (18)$$
$$\delta = \frac{\Delta}{\Delta_0}, \quad \nu = \frac{\mu}{\kappa\Delta_0}, \quad \mathbf{p} = \frac{\kappa v_F}{2\Delta_0}\mathbf{q}.$$

Similarly, for the nesting vector, we have $\mathbf{Q} = \mathbf{Q}_0 + 2\Delta_0\mathbf{p}/v_F\kappa$, where

$$\begin{pmatrix} p_x \\ p_y \end{pmatrix} = \int_0^{2\pi}\frac{d\varphi}{2\pi}\begin{pmatrix}\sin\varphi\\ \cos\varphi\end{pmatrix}\mathrm{sgn}[\nu_0(\mathbf{p},\varphi)-\nu] \quad (19)$$
$$\times\,\mathrm{Re}\sqrt{[\nu_0(\mathbf{p},\varphi)-\nu]^2-\delta^2}.$$

The relation between the chemical potential and the electron density can be found in the same way as above (see Eq. (8) and the text before it). As a result, we obtain [14]

$$\frac{x}{x_0} = \tilde{n}\nu - \int_0^{2\pi}\frac{d\varphi}{2\pi}\mathrm{sgn}[\nu_0(\mathbf{p},\varphi)-\nu]$$
$$\times\,\mathrm{Re}\sqrt{[\nu_0(\mathbf{p},\varphi)-\nu]^2-\delta^2},$$

where

$$x_0 = \frac{2v_0k_F^2\Delta_0}{\pi\kappa\epsilon_F}, \quad \tilde{n} = \frac{(v_{2F}^h)^{-1}+(v_{3F}^h)^{-1}+(v_F^e)^{-1}}{(v_F^h)^{-1}+(v_{2F}^e)^{-1}}, \quad (20)$$

v_0 is the unit cell volume, and $\tilde{n}$ is the electron density in nonmagnetic bands. Since $x_0 \sim \Delta_0/\epsilon_F \ll 1$, the phases arising in the system at $x \sim x_0$ correspond to the low-doping regime.

The behavior of the functions $\Delta(x)$ and $q(x)$ is illustrated in Figs. 6a and 6b for $\tilde{n} = \kappa = 1$ at two different values of α. The numerical analysis demonstrates that the SDW state arises if $|\bar{\alpha}| < 2$. If $|x| < x_1^*$, the charge carriers introduced by doping go to the nonmagnetic bands. As a result, the order parameter is independent of x, and $q(x) = 0$. At $|x| > x_1^*$, electrons (holes) appear in the band E_2 (E_1). The SDW order becomes incommensurate, $q \neq 0$. The spin configurations for the incommensurate SDW are schematically shown in Figs. 6c and 6d.

The chemical potential $\mu(x)$ computed in [14] is plotted in Fig. 7 for three different values of the ellipticity $\bar{\alpha}$ and at $\tilde{n} = \kappa = 1$. If $\bar{\alpha}$ is not large, then the function $\mu(x)$ is nonmonotonic and multivalued near $x = x_1^*$ (see Fig. 7a). At a larger ellipticity, the multivaluedness of $\mu(x)$ disappears (see Fig. 7b); then, at even larger $\bar{\alpha}$ values, the nonmonotonic behavior also disappears (see Fig. 7c). Thus, if the ellipticity is not too large, there are finite ranges of doping where

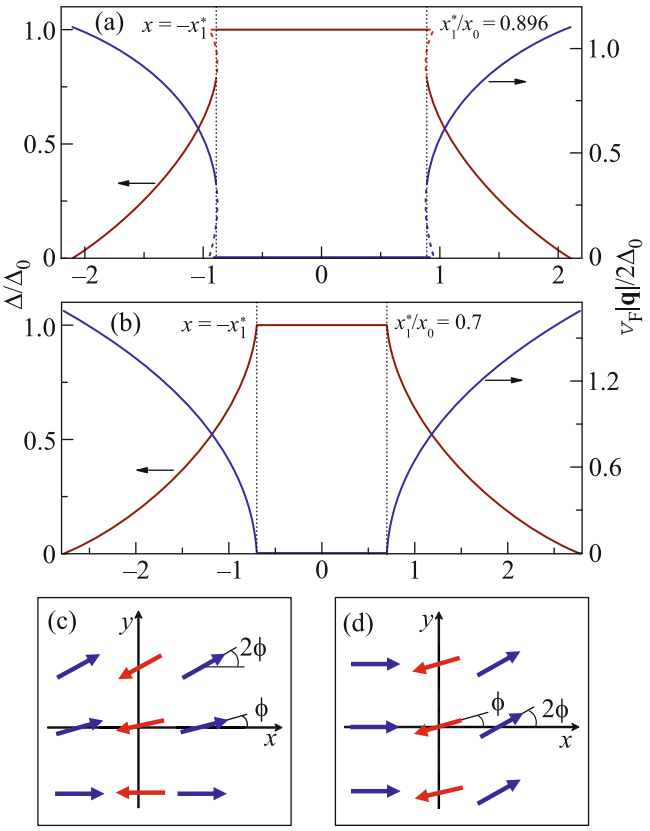

Fig. 6. (Color online) Δ and $|\mathbf{q}|$ versus x at $\tilde{n} = \kappa = 1$: (a) $\bar{\alpha} = 0.1$, the transition from the commensurate to incommensurate SDW state is of the first order; dashed lines depict the functions $\Delta(x)$ and $|\mathbf{q}(x)|$ corresponding to metastable states; (b) $\bar{\alpha} = 0.6$, the transition from commensurate to incommensurate SDW state is of the second order. Panels (c) and (d) show the schematics of the incommensurate SDW spin structure. If $\alpha > 0$, then panel (c) corresponds to the hole doping ($x < 0$) and panel (d) corresponds to the electron doping ($x > 0$). If $\alpha < 0$, then panel (c) corresponds to the electron doping, while panel (d) corresponds to the hole doping (Fig. 2 from [14]).

$\partial\mu(x)/\partial x < 0$, and the homogeneous state is unstable with respect to the separation into two phases. The phase separation range $x_1 < x < x_2$ shrinks if the ellipticity increases and disappears at the critical value $\bar{\alpha}_c = 1.15$.

In the phase-separated state, there exist two phases: phase 1 with a lower charge carrier density is the commensurate one and phase 2 with a higher charge carrier density corresponds to the incommensurate SDW state. The phase diagram of the system can be constructed following the approach described in the previous sections. The results obtained are summarized in the phase diagram in the (x,α) plane shown in Fig. 8 [14]. This phase diagram is calculated for $\tilde{n} = \kappa = 1$. It remains qualitatively the same if $\tilde{n} \neq 0$. If the nonmagnetic bands are absent, the

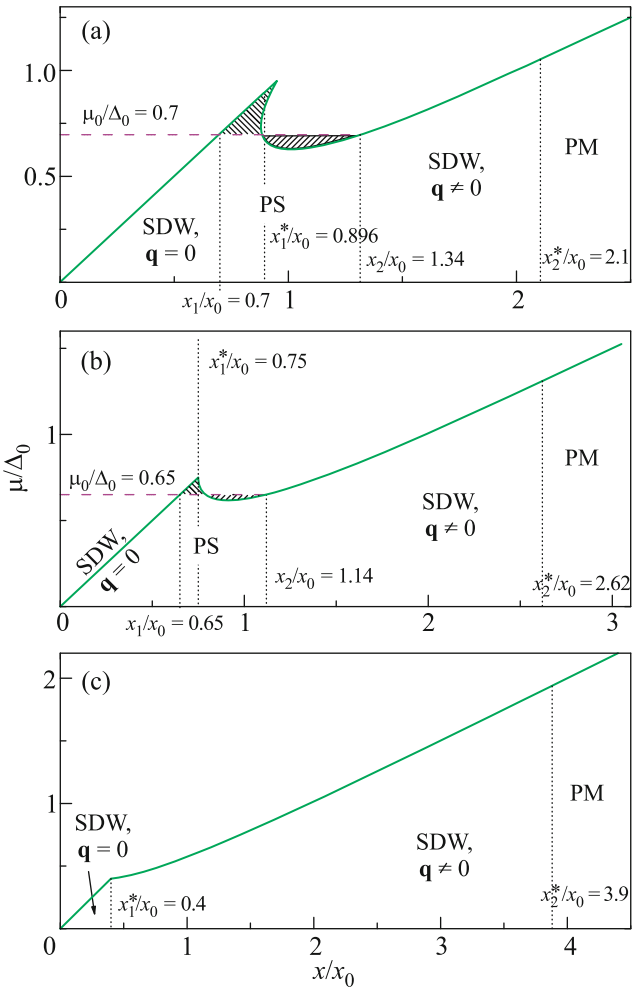

Fig. 7. (Color online) Chemical potential $\mu(x)$ calculated at $\bar{\alpha}$ = (a) 0.1, (b) 0.5, and (c) 1.2. Here, we have $\tilde{n} = \kappa = 1$. Panels (a) and (b) show that the homogeneous state is unstable with respect to phase separation if $x_1 < x < x_2$. The dashed (red) curve corresponds to the μ_0 value found using the Maxwell construction. The shaded areas above and below μ_0 are equal to each other. In panel (c), the chemical potential increases monotonically with x and no phase separation appears. The homogeneous commensurate and incommensurate SDW, paramagnetic (PM), and inhomogeneous commensurate–incommensurate SDW (PS) states are separated by vertical dashed lines (Fig. 3 from [14]).

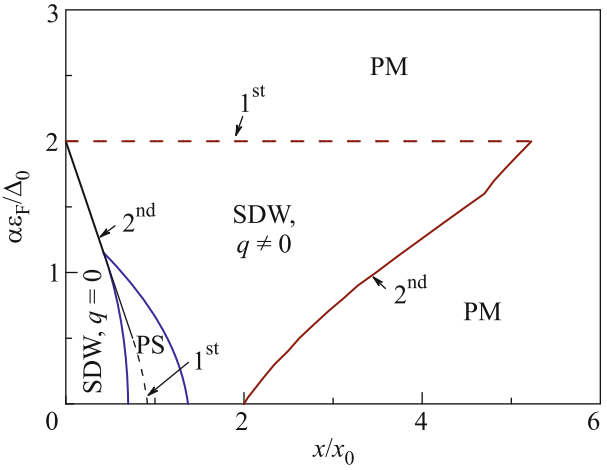

Fig. 8. (Color online) Phase diagram of the model for pnictides in the $(x, \bar{\alpha})$ plane, for $\tilde{n} = \kappa = 1$ and $\alpha, x > 0$. It is symmetric with respect to the replacement $x \to -x$ and/or $\alpha \to -\alpha$. The boundary between incommensurate SDW and paramagnetic (PM) states shown by the dashed (red) curve and by the solid (red) curve corresponds to the first- and second-order phase transitions, respectively. Solid (blue) lines indicate the boundaries of the phase-separated (PS) state. The solid (black) curve (second-order transition) and dashed (black) curve (first-order transition) show the boundaries between commensurate and incommensurate homogeneous SDW phases (Fig. 4 from [14]).

homogeneous commensurate SDW phase exists only when $x = 0$.

The phase separation in iron-based superconductors has been observed in several experiments [28–31]. For example, the inhomogeneous state with a commensurate AFM order and nonmagnetic domains with characteristic sizes about 65 nm was observed in the hole-doped $Ba_{1-x}K_xFe_2As_2$ compound [28]. The model described above predicts that the second phase is an incommensurate SDW phase rather than a nonmagnetic one. However, the thermodynamic potentials of the incommensurate SDW and metastable PM phases are very close to each other. The incommensurate SDW phase can be destroyed by an additional mechanism disregarded in the model, e.g., by disorder. In this case, the inhomogeneous state can be treated as a mixture of the commensurate SDW and paramagnetic phases.

Here, we consider the SDW order parameter in form (3). As was mentioned above, different order parameters are also discussed in the literature (see, e.g., [23]). However, the difference in the free energy corresponding to different kinds of order parameters is small. Therefore, the specific form of the order parameter is determined by the detailed characteristics of the system under study.

The calculations above show that there are only two possible equilibrium directions of the vector $\mathbf{q}$ characterizing the incommensurate SDW phase. This vector can be either parallel or perpendicular to the nesting vector $\mathbf{Q}_0$, depending on the type of doping and the sign of the ellipticity parameter α. It is clear that both the magnitude and the direction of $\mathbf{q}$ are sensitive to the shape of the Fermi surface. In actual pnictides, the shape of the hole pockets deviates from perfect circles and the spectrum of the bands depends on the transverse momentum k_z. Nevertheless, the observation of the incommensurate SDW phase with $\mathbf{q}$ perpendicular to $\mathbf{Q}_0$ in the electron-doped $Ba(Fe_{1-x}Co_x)_2As_2$ com-

pound was reported in [36–38], whereas the spin fluctuations corresponding to $\mathbf{q}$ parallel to $\mathbf{Q}_0$ have been observed in the hole-doped $Ba_{1-x}K_xFe_2As_2$ compound. These observations are in agreement with the prediction of the model.

Thus, the discussed model with a simple approximation of the Fermi surface predicts the existence of electronic phase separation in pnictides even in the weak-coupling regime. This is an important finding for the interpretation of the experimental data on phase inhomogeneity of iron pnictides: it proves that a purely electronic model with moderate interaction is sufficient to explain the observed inhomogeneous phases.

5. PHASE SEPARATION IN BILAYER AA GRAPHENE

Graphene is a zero-gap semiconductor exhibiting a host of unusual electronic characteristics [39]. In addition to single-layer graphene, bilayer graphene is also actively studied [40]. Bilayer graphene exists in three stacking modifications. The most common is the so-called Bernal, or AB, stacking of bilayer graphene. In the AB stacking, half of the carbon atoms in the top layer are located above the hexagon centers in the lower layer, and another half of the atoms in the top layer lie above the atoms in the lower layer. A different layer arrangement in which carbon atoms in the upper layer are located above the equivalent atoms of the bottom layer is referred to as AA-stacked bilayer graphene. The third modification is a twisted bilayer in which the top graphene layer is rotated by some angle with respect to the bottom layer. If the angle of rotation is not large, the twisted bilayer graphene can be approximately treated as a mixture of AB and AA stackings.

The unit cell of the bilayer graphene consists of four carbon atoms which form sublattices $A1$ and $B1$ in the bottom layer and $A2$ and $B2$ in the top layer. The tight-binding analysis shows that the AA bilayer has four bands (two hole bands and two electron bands) [40]:

$$\varepsilon_{\mathbf{k}}^{1,2} = -t_0 \pm t|f_{\mathbf{k}}|, \quad \varepsilon_{\mathbf{k}}^{3,4} = t_0 \pm t|f_{\mathbf{k}}|,$$
$$f_{\mathbf{k}} = 1 + \exp\left(\frac{3ik_xa_0}{2}\right)\cos\left(\frac{\sqrt{3}k_ya_0}{2}\right), \qquad (21)$$

where t_0 and t are the hopping amplitudes of electrons between the nearest carbon atoms in different layers and within the same layer, respectively, and a_0 is the lattice constant.

Band structure (21) is illustrated in Fig. 9. The low-energy dispersion in the AA bilayer is linear, similar to that of monolayer graphene. Unlike the latter, however, the AA bilayer has the Fermi surface including two valleys located near the Dirac points. An important feature of the AA bilayer is that the hole and electron Fermi surfaces coincide in the undoped material; i.e., there exists a perfect nesting, which becomes imperfect with doping. Then, even a weak electron–electron coupling gives rise to the SDW instability, to the formation of the AFM commensurate and incommensurate ordering, and to the phase separation [16, 40, 41]. Note that these properties are rather robust in the structures with the AA stacking. They also survive for the systems with longer-range hoppings and with nonequivalent layers [41].

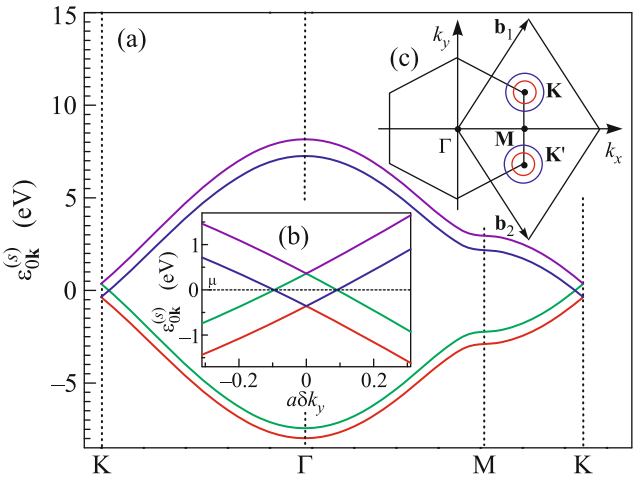

Fig. 9. (Color online) (a) Single-particle band structure of the AA-stacked bilayer graphene. (b) $\varepsilon_{\mathbf{k}}^{s}$ spectrum near the Dirac point located at the momentum $\mathbf{K}$. Here, $\mathbf{k} = \mathbf{K} + \delta k_y \mathbf{e}_y$. The intersection of the bands $s = 2$ and 3 occurs at zero energy, which corresponds to the Fermi level of the undoped system. (c) First Brillouin zone (hexagon) and the reciprocal-lattice unit cell (rhombus) of the AA bilayer graphene. The circles around points $\mathbf{K}$ and $\mathbf{K}'$ correspond to the Fermi surfaces of the doped system (Fig. 1 from [16]).

Thus, the existence of two bands with identical Fermi surfaces makes the AA-stacked bilayer graphene unstable with respect to spontaneous symmetry breaking. This instability can open a gap in the electronic spectrum, thus decreasing the free energy of the system for arbitrarily weak electron–electron interaction. The studies [15, 16, 41] have demonstrated that, for parameters characteristic of graphene-based systems, the ground state is the so-called G-type AFM order (all nearest neighboring spins in the lattice are antiparallel to each other). The AFM phase is mainly controlled by the on-site Coulomb repulsion. Let us analyze this problem in the framework of the Hubbard model with the electron–electron interaction term in the form

$$\hat{H}_{\text{int}} = \frac{U_0}{2}\sum_{\mathbf{m},i,\alpha,\sigma}\left(n_{\mathbf{m}i\alpha\sigma} - \frac{1}{2}\right)\left(n_{\mathbf{m}i\alpha\bar{\sigma}} - \frac{1}{2}\right), \qquad (22)$$

where $n_{\mathbf{m}i\alpha\sigma}$ is the particle number operator at site $\mathbf{m}$, $\alpha = A, B$ is the index of the sublattice, $i = 1, 2$ is the number of the graphene layer, and $\bar{\sigma}$ means "not σ." The intersite Coulomb interactions are neglected. In this case, it is commonly accepted that, for more adequate description of the actual situation, one should use a value of U_0 smaller than that predicted by the ab initio calculations. The estimate yields $U_0 = 5$–7 eV [40].

The commensurate AFM order parameter can be written as

$$\Delta_{iA} = U_0 \left\langle a^{\dagger}_{\mathbf{m}i\uparrow} a_{\mathbf{m}i\downarrow} \right\rangle, \quad \Delta_{iB} = U_0 \left\langle b^{\dagger}_{\mathbf{m}i\uparrow} b_{\mathbf{m}i\downarrow} \right\rangle, \quad \Delta_{1A} = \Delta_{2B} = -\Delta_{2A} = -\Delta_{1B} = \Delta, \tag{23}$$

Δ being a real parameter.

The mean-field band spectra have the form

$$\varepsilon^{1,4}_{\mathbf{k}} = \mp\sqrt{\Delta^2 + (t|f_{\mathbf{k}}| + t_0)^2}, \quad \varepsilon^{2,3}_{\mathbf{k}} = \mp\sqrt{\Delta^2 + (t|f_{\mathbf{k}}| - t_0)^2}. \tag{24}$$

To determine Δ, one has to minimize the corresponding grand potential

$$\Omega = \frac{4\Delta^2}{U_0} - U_0(n^2 - 1) - 2T \times \sum_{s=1}^{4} \int \frac{d\mathbf{k}}{V_{\mathrm{BZ}}} \ln\left[1 + \exp\frac{\mu' - \varepsilon^s_{\mathbf{k}}}{T}\right], \tag{25}$$

where n is the number of electrons per site, $x = n - 1$ is the doping level, V_{BZ} is the volume of the Brillouin zone, and $\mu' = \mu - U_0 x/2$. The calculated AFM gap decreases monotonically with the growth of the doping level x. The gap vanishes at some $x = x_c(T)$ [40].

The G-type AFM state has the lowest value of the thermodynamic potential among states with a commensurate magnetic order. Further optimization of Ω can be achieved if we take into account an incommensurate SDW ordering. Following [40], we represent the complex order parameter for this state in the form

$$\Delta_{\mathbf{n}iA} = e^{i\mathbf{q}\mathbf{n}}\Delta_{iA}, \qquad \Delta_{\mathbf{n}iB} = e^{i\mathbf{q}\mathbf{n}}\Delta_{iB}, \tag{26}$$

where $\mathbf{q}$ describes the spatial variation of the direction of the AFM vector; $\mathbf{S}_{\mathbf{n}i\alpha}$ is the averaged electron spin per unit cell $\mathbf{n}$ in the ith layer located at the sublattice α; it lies in the (x, y) plane and is related to the order parameter by $\mathbf{S}_{\mathbf{n}i\alpha} = \Delta_{i\alpha}[\cos\mathbf{q}\mathbf{n}, \sin\mathbf{q}\mathbf{n}]/U_0$.

Then, we should minimize Ω with respect to the $\mathbf{q}$ vector. The corresponding calculations are reported in [16]. The incommensurate AFM ordering exists in a slightly wider doping range than the commensurate one.

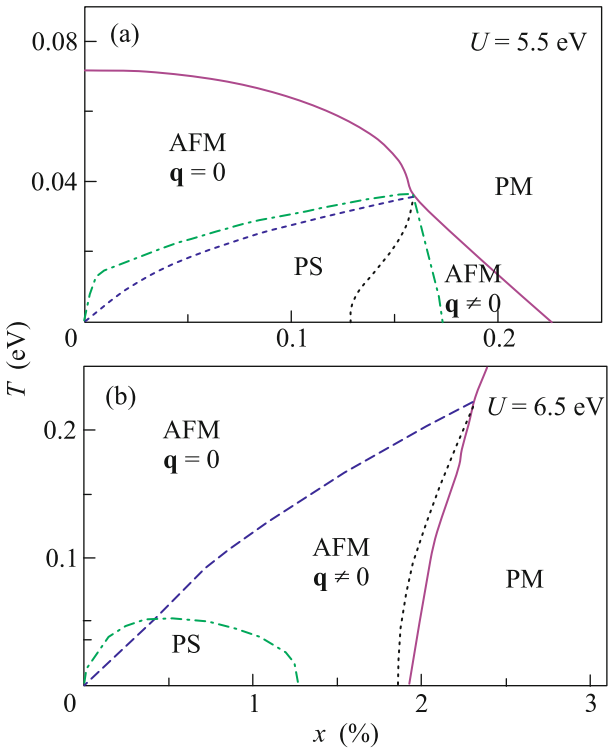

Fig. 10. (Color online) Phase diagram of the AA bilayer graphene calculated for U_0 = (a) 5.5 and (b) 6.5 eV. Solid (red) curves correspond to the transition temperature $T_{\mathrm{MF}}(x)$ between the AFM and paramagnetic states; (blue) dashed curves are the temperature $T^q(x)$ at which the transition between the commensurate and incommensurate AFM phases occurs. The dotted (black) curves correspond to the temperature $T_{\mathrm{MF}}(x)$ calculated disregarding the existence of the incommensurate AFM phase. The dash-dotted (green) curves are the boundaries of the phase-separation region (Fig. 32 from review [40]).

The formation of inhomogeneous states turns out to be an inherent feature of the multiband systems, especially of those with nesting. In [15, 16], it was predicted that the AA bilayer graphene at nonzero doping can become separated into two phases with unequal charge carrier densities $n_{1,2} = 1 + x_{1,2}$. It was demonstrated that a typical doping dependence of the chemical potential of AA graphene bilayer has the form shown in Fig. 1 for both commensurate and incommensurate AFM ordering if the onsite Coulomb repulsion is not too strong, $U_0 < \pi\sqrt{3}t^2/t_0$. This indicates that the system is unstable and can undergo the phase separation into commensurate ($\mathbf{q} = 0$, $x_1 < x$) and incommensurate ($\mathbf{q} \neq 0$, $x_2 > x$) phases. The phase diagram of the AA graphene bilayer in the (x, T) plane is shown in Fig. 10 for two different values of U_0. The region of phase separation is bounded by dash-dotted (green) curves. Note that the incommensurate order is known to be sensitive to disorder. Moreover, the grand

potential difference for incommensurate and commensurate AFM phases is not large. Thus, the phase separation involving the AFM insulator ($x_1 = 0$) and the paramagnetic (if $U_0 > 6$ eV) or AFM (if $U_0 < 6$ eV) metal is quite possible. Note also that the phase separation will be frustrated by the long-range Coulomb repulsion since the local charge neutrality is broken in the inhomogeneous phase. The phase separation region shrinks with the growth of U_0 on the doping axis, while the temperature range where the phase separation is possible increases with U_0. However, one should remember that the mean-field approach is not a good approximation in the case of large U_0 values.

6. CONCLUSIONS

Thus, the formation of inhomogeneous electron states (electronic phase separation) is a rather general feature of the systems with the imperfect nesting of the Fermi surface. Among the materials belonging to this class, we have chromium and its alloys, iron-based pnictide superconductors, and graphene related materials, as well as some other materials which we have not touched upon in this review, such as hexaborides and organic metals and also other interesting and widely studied compounds.

This work was supported by the Russian Foundation for Basic Research, project nos. 14-02-00276, 17-02-00135, and 17-02-00323. M.Yu.K. acknowledges the support from the Program of Basic Research of the National Research University Higher School of Economics.

REFERENCES

1. D. Khomskii, *Basic Aspects of the Quantum Theory of Solids* (Cambridge Univ. Press, Cambridge, 2010).
2. G. Grüner, Rev. Mod. Phys. **60**, 1129 (1988).
3. P. Monceau, Adv. Phys. **60**, 325 (2012).
4. A. W. Overhauser, Phys. Rev. **128**, 1437 (1962).
5. G. Grüner, Rev. Mod. Phys. **66**, 1 (1994).
6. J. Ruvalds, C. T. Rieck, S. Tewari, J. Thoma, and A. Virosztek, Phys. Rev. B **51**, 3797 (1995).
7. A. Gabovich, A. Voitenko, J. Annett, and M. Ausloos, Supercond. Sci. Technol. **14**, R1 (2001).
8. K. Terashima, Y. Sekiba, J. Bowen, K. Nakayama, T. Kawahara, T. Sato, P. Richard, Y.-M. Xu, L. J. Li, G. H. Cao, Z.-A. Xu, H. Ding, and T. Takahashi, Proc. Natl. Acad. Sci. **106**, 7330 (2009).
9. A. Shibatani, J. Phys. Soc. Jpn. **26**, 299 (1969).
10. A. Shibatani, K. Motizuki, and T. Nagamiya, Phys. Rev. **177**, 984 (1969).
11. A. Shibatani, J. Phys. Soc. Jpn. **29**, 93 (1970).
12. T. M. Rice, Phys. Rev. B **2**, 3619 (1970).
13. A. L. Rakhmanov, A. V. Rozhkov, A. O. Sboychakov, and F. Nori, Phys. Rev. B **87**, 075128 (2013).
14. A. O. Sboychakov, A. V. Rozhkov, K. I. Kugel, A. L. Rakhmanov, and F. Nori, Phys. Rev. B **88**, 195142 (2013).
15. A. O. Sboychakov, A. L. Rakhmanov, A. V. Rozhkov, and F. Nori, Phys. Rev. B **87**, 121401 (2013).
16. A. O. Sboychakov, A. V. Rozhkov, A. L. Rakhmanov, and F. Nori, Phys. Rev. B **88**, 045409 (2013).
17. A. Narayanan, A. Kiswandhi, D. Graf, J. Brooks, and P. Chaikin, Phys. Rev. Lett. **112**, 146402 (2014).
18. G. Campi, A. Bianconi, N. Poccia, G. Bianconi, L. Barba, G. Arrighetti, D. Innocenti, J. Karpinski, N. D. Zhigadlo, S. M. Kazakov, M. Burghammer, M. V. Zimmermann, M. Sprung, and A. Ricci, Nature **525**, 359 (2015).
19. R. Chen, B. Hu, T. Dong, and N. L. Wang, Phys. Rev. B **89**, 075114 (2014).
20. E. Fawcett, Rev. Mod. Phys. **60**, 209 (1988).
21. P. Fulde and R. A. Ferrell, Phys. Rev. **135**, A550 (1964).
22. A. I. Larkin and Yu. N. Ovchinnikov, Sov. Phys. JETP **20**, 762 (1964); A. I. Larkin, *Collection of Works* (MTsNMO, Moscow, 2014), Vol. 1, p. 181 [in Russian].
23. L. P. Gor'kov and G. B. Teitel'baum, Phys. Rev. B **82**, 020510 (2010).
24. D. E. Sheehy and L. Radzihovsky, Ann. Phys. **322**, 1790 (2007).
25. S. Takada, Progr. Theor. Phys. **43**, 27 (1970).
26. A. O. Sboychakov, A. L. Rakhmanov, K. I. Kugel, A. V. Rozhkov, and F. Nori, Phys. Rev. B **95**, 014203 (2017).
27. P. Dai, J. Hu, and E. Dagotto, Nat. Phys. **8**, 709 (2012).
28. J. T. Park, D. Inosov, C. Niedermayer, G. L. Sun, D. Haug, N. B. Christensen, R. Dinnebier, A. V. Boris, A. J. Drew, L. Schulz, T. Shapoval, U. Wolff, V. Neu, X. Yang, C. T. Lin, B. Keimer, and V. Hinkov, Phys. Rev. Lett. **102**, 117006 (2009).
29. D. Inosov, A. Leineweber, X. Yang, J. T. Park, N. B. Christensen, R. Dinnebier, G. L. Sun, Ch. Niedermayer, D. Haug, P. W. Stephens, J. Stahn, C. T. Lin, O. K. Andersen, B. Keimer, and V. Hinkov, Phys. Rev. B **79**, 224503 (2009).
30. G. Lang, H.-J. Grafe, D. Paar, F. Hammerath, K. Manthey, G. Behr, J. Werner, and B. Büchner, Phys. Rev. Lett. **104**, 097001 (2010).
31. B. Shen, B. Zeng, G. Chen, J. B. He, D. M. Wang, H. Yang, and H. H. Wen, Europhys. Lett. **96**, 37010 (2011).
32. Q. Luo, G. Martins, D.-X. Yao, M. Daghofer, R. Yu, A. Moreo, and E. Dagotto, Phys. Rev. B **82**, 104508 (2010).
33. G. Stewart, Rev. Mod. Phys. **83**, 1589 (2011).

34. A. Ricci, N. Poccia, G. Campi, B. Joseph, G. Arrighetti, L. Barba, M. Reynolds, M. Burghammer, H. Takeya, Y. Mizuguchi, Y. Takano, M. Colapietro, N. L. Saini, and A. Bianconi, Phys. Rev. B **84**, 060511 (2011).
35. A. Ricci, N. Poccia, B. Joseph, G. Arrighetti, L. Barba, J. Plaisier, G. Campi, Y. Mizuguchi, H. Takeya, Y. Takano, N. L. Saini, and A. Bianconi, Supercond. Sci. Technol. **24**, 082002 (2011).
36. P. Bonville, F. Rullier-Albenque, D. Colson, and A. Forget, Europhys. Lett. **89**, 67008 (2010).
37. Y. Laplace, J. Bobroff, F. Rullier-Albenque, D. Colson, and A. Forget, Phys. Rev. B **80**, 140501 (2009).
38. D. Pratt, M. Kim, A. Kreyssig, Y. B. Lee, G. S. Tucker, A. Thaler, W. Tian, J. L. Zarestky, S. L. Bud'ko, P. C. Canfield, B. N. Harmon, A. I. Goldman, and R. J. McQueeney, Phys. Rev. Lett. **106**, 257001 (2011).
39. A. C. Neto, F. Guinea, N. M. Peres, K. S. Novoselov, and A. K. Geim, Rev. Mod. Phys. **81**, 109 (2009).
40. A. Rozhkov, A. Sboychakov, A. Rakhmanov, and F. Nori, Phys. Rep. **648**, 1 (2016).
41. A. Rakhmanov, A. Rozhkov, A. Sboychakov, and F. Nori, Phys. Rev. Lett. **109**, 206801 (2012).

Translated by K. Kugel